



Article

Moss-like Hierarchical Architecture Self-Assembled by Ultrathin $\text{Na}_2\text{Ti}_3\text{O}_7$ Nanotubes: Synthesis, Electrical Conductivity, and Electrochemical Performance in Sodium-Ion Batteries

Denis P. Opra, Anton I. Neumoin *, Sergey L. Sinebryukhov , Anatoly B. Podgorbunsky , Valery G. Kuryavyi, Vitaly Yu. Mayorov, Alexander Yu. Ustinov and Sergey V. Gnedenkov

Institute of Chemistry, Far Eastern Branch of the Russian Academy of Sciences, 690022 Vladivostok, Russia; dp.opra@ich.dvo.ru (D.P.O.); sls@ich.dvo.ru (S.L.S.); pab@ich.dvo.ru (A.B.P.); kvg@ich.dvo.ru (V.G.K.); 024205@inbox.ru (V.Y.M.); all_vl@mail.ru (A.Y.U.); svg21@hotmail.com (S.V.G.)

* Correspondence: anton_neumoin@ich.dvo.ru; Tel.: +7-(924)-338-8153



Citation: Opra, D.P.; Neumoin, A.I.; Sinebryukhov, S.L.; Podgorbunsky, A.B.; Kuryavyi, V.G.; Mayorov, V.Y.; Ustinov, A.Y.; Gnedenkov, S.V. Moss-like Hierarchical Architecture Self-Assembled by Ultrathin $\text{Na}_2\text{Ti}_3\text{O}_7$ Nanotubes: Synthesis, Electrical Conductivity, and Electrochemical Performance in Sodium-Ion Batteries. *Nanomaterials* **2022**, *12*, 1905. <https://doi.org/10.3390/nano12111905>

Academic Editor: Christian M. Julien

Received: 22 April 2022

Accepted: 29 May 2022

Published: 2 June 2022

Publisher's Note: MDPI stays neutral with regard to jurisdictional claims in published maps and institutional affiliations.



Copyright: © 2022 by the authors. Licensee MDPI, Basel, Switzerland. This article is an open access article distributed under the terms and conditions of the Creative Commons Attribution (CC BY) license (<https://creativecommons.org/licenses/by/4.0/>).

Abstract: Nanocrystalline layer-structured monoclinic $\text{Na}_2\text{Ti}_3\text{O}_7$ is currently under consideration for usage in solid state electrolyte applications or electrochemical devices, including sodium-ion batteries, fuel cells, and sensors. Herein, a facile one-pot hydrothermal synthetic procedure is developed to prepare self-assembled moss-like hierarchical porous structure constructed by ultrathin $\text{Na}_2\text{Ti}_3\text{O}_7$ nanotubes with an outer diameter of 6–9 nm, a wall thickness of 2–3 nm, and a length of several hundred nanometers. The phase and chemical transformations, optoelectronic, conductive, and electrochemical properties of as-prepared hierarchically-organized $\text{Na}_2\text{Ti}_3\text{O}_7$ nanotubes have been studied. It is established that the obtained substance possesses an electrical conductivity of 3.34×10^{-4} S/cm at room temperature allowing faster motion of charge carriers. Besides, the unique hierarchical $\text{Na}_2\text{Ti}_3\text{O}_7$ architecture exhibits promising cycling and rate performance as an anode material for sodium-ion batteries. In particular, after 50 charge/discharge cycles at the current loads of 50, 150, 350, and 800 mA/g, the reversible capacities of about 145, 120, 100, and 80 mA·h/g, respectively, were achieved. Upon prolonged cycling at 350 mA/g, the capacity of approximately 95 mA·h/g at the 200th cycle was observed with a Coulombic efficiency of almost 100% showing the retention as high as 95.0% initial storage. At last, it is found that residual water in the un-annealed nanotubular $\text{Na}_2\text{Ti}_3\text{O}_7$ affects its electrochemical properties.

Keywords: hierarchical materials; nanotubes; mesoporosity; sodium trititanate; hydrothermal synthesis; conductivity; sodium-ion batteries

1. Introduction

Recently, functional materials with a hierarchical architecture constructed by unique assemblies of constituent elements have gained increased attention. If such organized multilevel architectures are formed spontaneously, the process is called “self-assembling”. The character of structural integration is determined by difference in the nature of interaction forces due to which the formation of levels occurs. [1,2]. The topological benefits of hierarchical materials can provide unusual functionalities making them valuable for practical applications.

Titanium compounds are applied in a wide range of applications including paints, catalysts, plastics, coatings, sensors, hygienic products, cosmetics, pharmaceuticals, and even foods [3–8]. Yearly world titanium demand (in TiO_2 -units) is estimated around 6 million tons growing by about 3% per year [9–11]. Furthermore, titanium compounds are already applied in battery production (e.g., spinel $\text{Li}_4\text{Ti}_5\text{O}_{12}$ that is valuable anode material for lithium storage due to its advantageous properties in long-term cycling stability) [12–15]. Looking forward to years to come, the manufacturers focus today on the

development advanced energy-storage strategies based on cheaper and abundant chemicals, such as sodium-ion batteries (SIBs). One of the key challenges, hampering the SIBs commercialization, is an absence of electrode materials capable to provide required electrochemical performance but maintaining, at the same time, economic competitiveness of this technology [16,17]. Recently, transition metal oxides [18], sulfides [19], fluorides [20], phosphates [21,22], selenides [23], and nitrides [24] have been investigated as electrode materials for SIBs. Among the titanium-containing compounds, $\text{Na}_2\text{Ti}_6\text{O}_{13}$, $\text{NaTi}_2(\text{PO}_4)_3$, NaTiO_2 , TiO_2 , $\text{Na}_2\text{Ti}_4\text{O}_9$, ATiOPO_4 ($A = \text{NH}_4, \text{K}, \text{Na}$), and $\text{Na}_2\text{Ti}_3\text{O}_7$ turned out to be the most promising for usage as active materials in SIBs electrodes [25–28]. The benefits of $\text{Na}_2\text{Ti}_3\text{O}_7$ include high ionic conductivity, proper sodium storage capacity (177 mA·h/g) and suitable potential (0.2–0.3 V; can be applied as the anode material), moderate volume changes (~6%; it is less than for carbonaceous anode in LIBs (9–12%)) upon sodiation/desodiation [29,30].

This work aims to develop a facile one-pot method for preparing $\text{Na}_2\text{Ti}_3\text{O}_7$ with a hierarchical architecture using a hydrothermal technology that meets the requirements of scalability as well as to study the features of morphology and texture, conductive, optical, electronic, and electrochemical properties of that as-prepared materials.

2. Materials and Methods

All reagents for experiments in this work had an analytical grade and used without further purification. Nanotube-constructed mesoporous $\text{Na}_2\text{Ti}_3\text{O}_7$ microparticles similar to moss were prepared by a hydrothermal method through the treatment of TiO_2 P25 (99.7%, Sigma-Aldrich, St. Louis, MO, USA) in a highly alkaline medium. In a typical procedure, 0.4 g titanium dioxide was dispersed in a 20 mL aqueous solution of sodium hydroxide (10 M) under continuous stirring. The obtained suspension was transferred into a 25 mL Teflon-lined stainless-steel autoclave. The autoclave was placed in an oven and maintained at 130 °C for 36 h. After cooling to room temperature, the resulting white suspension was precipitated by centrifugation and then many times washed with deionized water until the pH became neutral. Finally, the product was dried at 120 °C in air for 12 h (un-annealed sample denoted as NTO-120). To determine the effect of temperature on physicochemical properties, the resulting product was next annealed at 250 °C (NTO-250), 350 °C (NTO-350), and 500 °C (NTO-500) in air for 3 h.

X-ray diffraction (XRD) was carried out using a Stadi P diffractometer (STOE, Darmstadt, Germany) with $\text{CuK}\alpha$ radiation ($\lambda = 1.5418 \text{ \AA}$) in the 2θ range of 5–60° (step of 0.024°). Identification of phases was performed in EVA version 2.0 software (Bruker, Billerica, MA, USA). The morphological characteristics of materials were studied by scanning (SEM) and scanning transmission (STEM) electron microscopy on Sigma 300 VP (Carl Zeiss, Oberkochen, Germany) and S5500 (Hitachi, Tokyo, Japan) microscopes. The analysis and processing of SEM images were performed in ImageJ program developed at the National Institutes of Health (Bethesda, MD, USA) by Wayne Rasband. The elemental composition and distributions of elements were studied by energy dispersive X-ray spectroscopy (EDX) on a Carl Zeiss Merlin microscope (Carl Zeiss, Oberkochen, Germany) equipped with EDX analyzer. Nitrogen adsorption–desorption tests were performed on the Quantachrome Autosorb iQ instrument (Anton Paar, Graz, Austria). The specific surface area, pore size distribution, and pore volume were estimated using a Brunauer-Emmett-Teller (BET) and Barrett-Joyner-Halenda (BJH) models. The chemical composition was studied by X-ray photoelectron spectroscopy (XPS) on a SPECS spectrometer (SPECS, Berlin, Germany) equipped with a hemispherical Phoibos-150 analyzer using $\text{MgK}\alpha$ radiation ($\lambda = 9.7349 \text{ \AA}$). The binding energy scale was calibrated using the position of C 1s peak at 285 eV. An ultraviolet-visible (UV-vis) UV2700Plus spectrophotometer (Shimadzu, Kyoto, Japan) was applied to study the electronic band structure. The experiments were carried out in the wavelength range from 200 to 800 nm. Barium sulfate was used as a reflection (white) standard. The electrophysical characteristics were investigated using a Solartron complex (Solartron Mobrey, Farnborough, Hampshire, UK) composed of SI 1260 impedance/gain-phase analyzer and 1296 dielectric interface. The materials were pressed into pellets with

a diameter of 10 mm and a thickness of 0.4–0.5 mm. To provide electrical contact, pellets were coated with a conductive Dotite D-550 Silver paste. Measurements were carried out in the frequency range from 1 Hz to 20 MHz with an amplitude of 0.5 V. The bulk resistance was calculated from the high-frequency region of impedance spectra using the equivalent electrical circuit (EEC) approach. Fitting was performed using a parallel RC-circuit.

The electrochemical characteristics of products were determined using two-electrode ECC-STD cells (EL-Cell, Hamburg, Germany). The slurry of working electrode was prepared by mixing 90 wt.% active material and 10 wt.% Tuball™ Bat NMP additive (OCSiAl, Leudelange, Luxemburg) in an appropriate amount of *N*-methylpyrrolidone. For rate capability experiments, the proportion of conductive component was adjusted to 20 wt.% by adding Super P acetylene black (Alfa Aesar, Ward Hill, MA, USA). The resulting slurry was spread in a uniform 50 µm thick layer onto an aluminium foil current collector using an AFA-III coater (MTI, Richmond, CA, USA). The foil was pre-treated in a dilute hydrochloric acid solution. The obtained electrode sheet was dried at 60 °C to a constant weight. Then, electrode disks with a diameter of 15 mm were cut out from the sheet using a GN-CP20 device (Gelon, Linyi, China). The electrochemical cells were assembled in an argon-filled glove box. Metallic sodium was used as the counter and reference electrodes. 1 M solution of NaClO₄ in propylene carbonate with the addition of fluoroethylene carbonate (5 vol.%) was applied as an electrolyte. A separator was a GF/C glass fiber from the Whatman (Little Chalfont, Buckinghamshire, UK). The half-cells were tested on a Solartron Analytical 1400 (Solartron Mobrey, Farnborough, Hampshire, UK) and Elins P-20X8 (Elins, Zelenograd, Russia). The measurements were conducted at room temperature in the potential range of 0.01–2.5 V (vs. Na/Na⁺). Galvanostatic charge/discharge cycling was carried out at current densities of 50, 150, and 350 mA/g. During discussions, despite applying half-cells, the charge designates a sodiation process, while the discharge implies desodiation. Cyclic voltammetry (CV) curves were recorded at a potential sweep rate of 50 µV/s. Electrochemical impedance spectroscopy (EIS) spectra were recorded in the frequency range of 10⁶–10^{−2} Hz with an ac amplitude of 10 mV at the potential of 0.01 V (i.e., at a fully sodiated state). The EIS-spectra were processed with Zview software from Scribner Associates (Southern Pines, NC, USA).

3. Results

3.1. Structure, Morphology, and Conductive Properties of Moss-like Hierarchical Structure Self-Assembled by Na₂Ti₃O₇ Nanotubes

To study the effect of annealing temperature on the phase composition of prepared Na₂Ti₃O₇ products, XRD studies were carried out. The XRD patterns for samples obtained at temperatures of 120, 250, 350, and 500 °C are illustrated in Figure 1. As it can be seen, the observed peaks in diffraction patterns are broadened presuming the nanocrystalline materials. The data show that the dominant crystal phase in NTO-120, NTO-250, and NTO-350 samples was sodium trititanate (PDF No. 59-0666) crystallizes in a monoclinic space group *P*2₁/*m* with the parameters: *a* = 9.3987 Å, *b* = 3.7566 Å, *c* = 11.0272 Å, β = 101.6°. Besides, anatase titanium dioxide (PDF No. 21-1272) was identified in the analyzed samples as phase impurity. Up to annealing at 350 °C, the XRD patterns (including position, geometry, and broadening of diffraction peaks) are the same, indicating an absence of distinguished changes. On the other hand, if the calcination at the temperature of 500 °C was carried out, it would result in the irreversible phase transformation of Na₂Ti₃O₇ to anatase, signed by strengthening of corresponding peaks. The obtained results are in agreement with the data of other researchers [31,32].

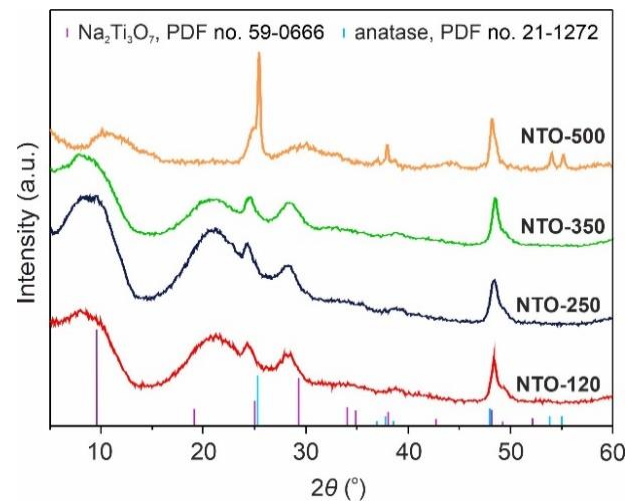


Figure 1. XRD patterns of $\text{Na}_2\text{Ti}_3\text{O}_7$ -based products prepared at different temperatures (120–500 °C) NTO-120, NTO-250, NTO-350, and NTO-500 products.

For the investigation into the microstructure of synthesized materials, SEM and STEM experiments were carried out. The results reveal that samples looked identically and have a self-assembled hierarchical architecture comprising two levels of organization. As an example, in Figure 2 and Figure S1 the morphology of NTO-120 and NTO-350 products is illustrated. It is found (SEM data; Figure 2a,b and Figure S1) that first level of hierarchy is formed by microparticles of 1–10 μm in diameter possessing a rough surface. The particles look similar to moss-like lichens, called “reindeer mosses” (Figure S2).

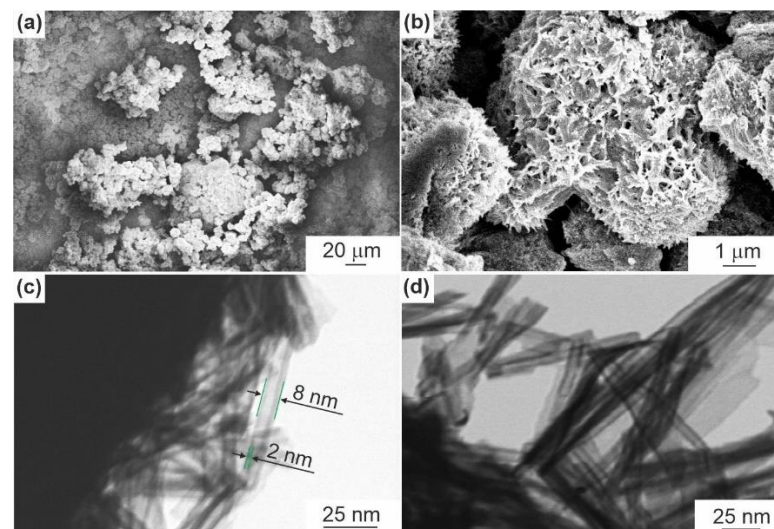


Figure 2. SEM-images show the microscale topography for NTO-120 sample at the magnifications of 300 \times (a) and 10,000 \times (b). STEM-imaging at the magnification of 700,000 \times reveals the structural hierarchy of NTO-120 (c) and NTO-350 (d) products.

An in-depth study (STEM mode; Figure 2c), shows that these microscale moss-like objects consist of smaller size one-dimensional hollow cylindrical nanostructures (i.e., nanotubes). The nanotubes are extremely uniform in size that is might be an important factor for usage as electrode-active materials for batteries. The outer diameter of these tubes varies in the range of 6–9 nm, the wall thickness does not exceed 2–3 nm (ultrathin). The length of nanotubes is equal to several hundred nanometers. The sample annealed at 350 °C (Figure 2d) did not demonstrate noticeable changes in microstructure, and no agglomerates of nanotubes were observed.

The EDX studies give an insight on elements in the samples. It is shown that synthesized materials contain O, Na, Ti, and C in trace amounts, as displayed in Figure 3a–e using NTO-120 as an example. The maps reveal a uniform distribution of oxygen, sodium, and titanium at the products surface, as well as carbon (Figure S3), the origin of which will be clarified later using XPS.

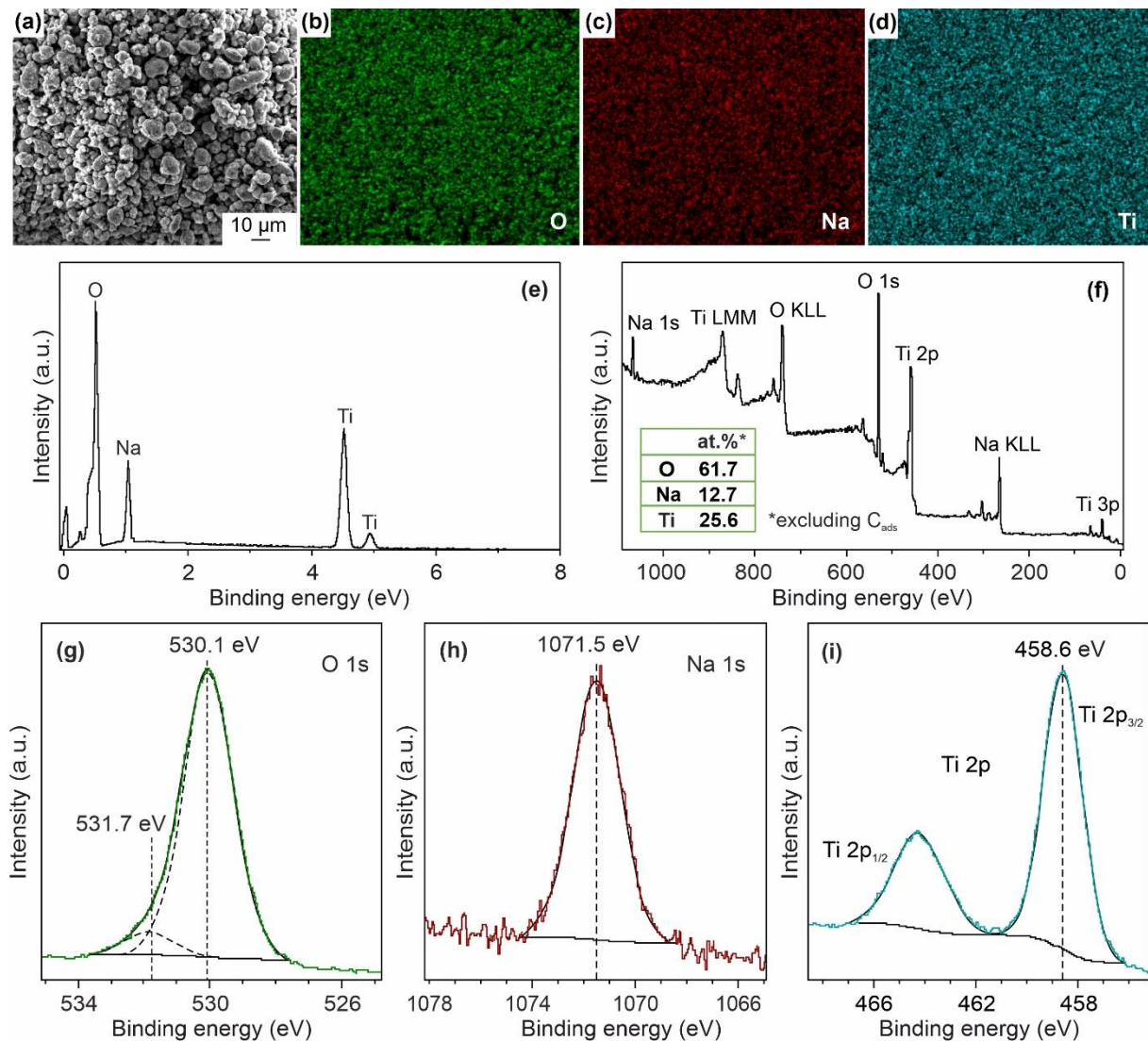


Figure 3. SEM-image of the analyzed area (a), corresponding elemental maps (b–d), and EDX-spectrum (e) for NTO-120 sample. XPS-spectra for the NTO-350 surface: survey scan (f), O 1s (g), Na 1s (h), Ti 2p (i). The inset in (f) shows the content of elements estimated from XPS peak areas.

To determine the chemical state of elements in the prepared materials, XPS experiments were performed. Figure 3 illustrated the XPS data obtained for the NTO-350 sample. The survey spectrum (Figure 3f) shows the presence of signals from Na, Ti, and O elements. The existence of carbon in XPS analyses is explained by the nanoscale morphology sensitive to environment contaminations [33,34]. In the photoelectron spectrum of O 1s (Figure 3g) two prominent peaks are detected at 530.1 eV (89%) and 531.7 eV (11%), which, respectively, associating with the oxygen bonded to metal and the oxygen of hydroxyl groups or carbonates (CO_3^{2-}) existed at the surface. The binding energy of Na 1s (Figure 3h) is 1071.5 eV. The Ti 2p core-level XPS spectrum (Figure 3i) shows spin-orbit doublet of $2p_{3/2}$ (458.6 eV) and $2p_{1/2}$ (464.2 eV) with a separation of 5.7 eV corresponding to the +4 oxidation state of titanium. The registered positions of peaks are in agreement with that from literature for

$\text{Na}_2\text{Ti}_3\text{O}_7$ [35]. The elemental composition of NTO-350 determined from XPS peak areas (Figure 3f, inset) corresponds to the $\text{Na}_{1.63}\text{Ti}_{3.28}\text{O}_{7.07}$ formula (ignoring the TiO_2 impurity), which is close to sodium trititanate.

To obtain information about texture of synthesized $\text{Na}_2\text{Ti}_3\text{O}_7$ materials, a low-temperature N_2 adsorption-desorption method was used. Figure 4 represents the experimental isotherms, pore volume data, and pore size distribution curves for NTO-120 and NTO-350 samples. It can be seen that products exhibited a type IV isotherms (in terms of the IUPAC classification) with the H3 hysteresis loops starting at p/p_0 of 0.43, which corresponds to the mesoporous materials. The pore size distribution profiles (insets in Figure 4) have narrow peaks at 5.68 nm (NTO-120) and 6.32 nm (NTO-350) further evidence that the mesoscopic scale porosity is the dominant in products. The total pore volume for samples can be estimated as 0.54–0.6 cm^3/g . The BET specific surface area changes from 313.9 to 282.8 m^2/g and the BJH pore volume varies between 0.54 and 0.60 cm^3/g during treatment at temperatures in the range of 120–350 °C. Thus, it can be concluded that the obtained materials are characterized by a large specific surface area and high pore volume with a pore network formed predominantly by mesoporous channels. Interestingly, the NTO-350 sample possesses some higher pore volume as opposed to the un-annealed product. This is likely caused by the opening of pores due to dehydration (Figure S4).

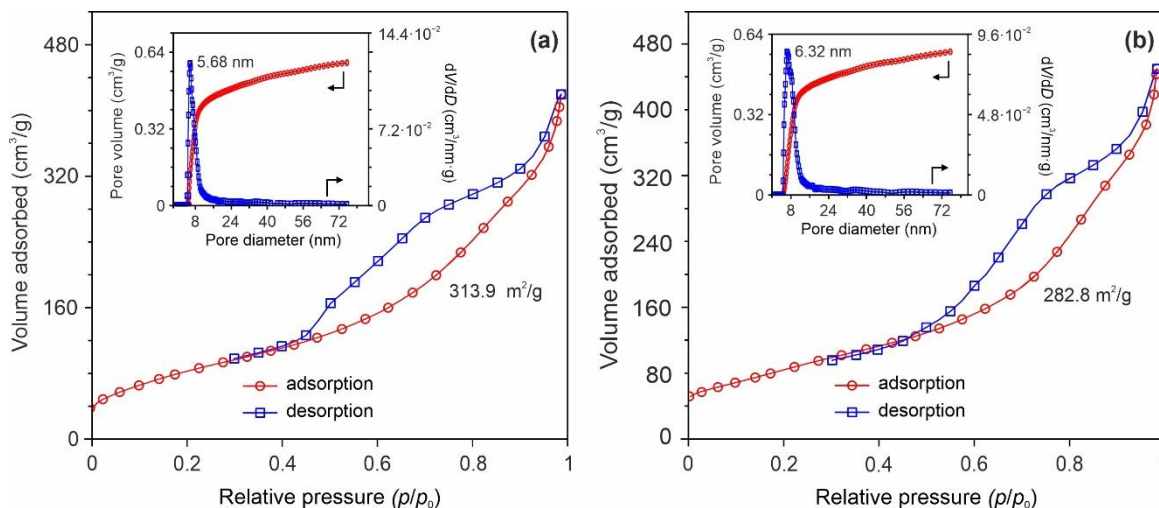


Figure 4. Data of adsorption measurements for NTO-120 (a) and NTO-350 (b) samples.

Table S1 summarizing the textural characteristics and preparing techniques for different nanostructured sodium trititanate demonstrates that the synthetic procedure in this work might be useful to design and fabricate functional $\text{Na}_2\text{Ti}_3\text{O}_7$ -based materials for various fields.

Figure 5a represents the UV-vis diffuse reflectance spectra of analyzed $\text{Na}_2\text{Ti}_3\text{O}_7$ materials. According to data, the samples absorb UV-rays and have high reflectance in the visible region ($\lambda > 400$ nm), demonstrating a typical behavior for $\text{Na}_2\text{Ti}_3\text{O}_7$, which is a wide-bandgap semiconductor. The optical band gap (E_g) of the products was estimated by Tauc relation (Equation (1)) for allowed indirect transitions ($\gamma = 2$) using a Kubelka–Munk model ($\alpha \sim F(R_\infty)$):

$$(\alpha \cdot \hbar\omega)^{1/\gamma} = A(\hbar\omega - E_g) \quad (1)$$

where α is the absorption coefficient, $\hbar\omega$ is the photon's energy, A is the constant called the band tailing parameter, $F(R_\infty) = (1 - R_\infty)^2/2R_\infty$ is the Kubelka–Munk function, and R_∞ is the reflectivity.

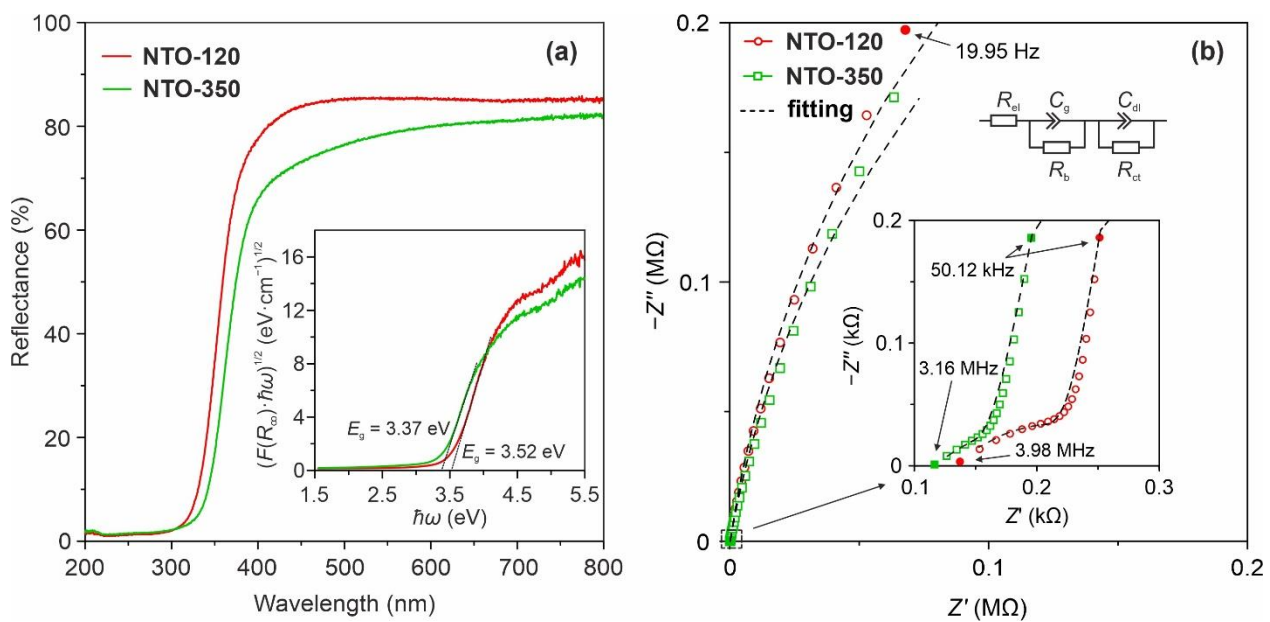


Figure 5. UV-vis diffuse reflection spectra (a) with the corresponding Tauc plots (inset) for band gap determination and impedance spectra (b) with the EEC used for fitting of NTO-120 and NTO-350 materials (to guide the reader's eye high-frequency regions of spectra are shown enlarged at the right).

In this way, the $(F(R_{\infty}) \cdot \hbar\omega)^{1/2}$ against $\hbar\omega$ graph is plotted and then a linear section of the curve is extrapolated to the x -axis (an intersection point gives the E_g). The Tauc plots of tested samples are shown in the inset of Figure 5a. According to estimations, the band gap of the NTO-120 sample is equal to 3.52 eV agreeing with the results of theoretical calculations (3.28 eV) [36,37] and experimental measurements (3.40–3.51 eV) [37–40] reported in the literature. Note that some authors had measured a larger band gap for $\text{Na}_2\text{Ti}_3\text{O}_7$ (3.7–3.85 eV) [41–43]. After annealing at 350 °C, the band gap decreases to 3.37 eV. Probably, this may be due to change in phase ratio resulting in the construction of the $\text{Na}_2\text{Ti}_3\text{O}_7$ /anatase heterojunction structure. Further experiments are required to study this question that goes beyond the scopes of the study. On the other hand, there are many experimental data and theoretical models indicating an increase in the band gap of semiconductor nanomaterials due to decreasing their particle size [44]. This is explained by the fact that in the nanoscale state in semiconductors, the quantum confinement effect of electrons and holes occurs, which leads to an energy difference between the filled states and the empty states. Therefore, as the particle size changes, the band gap either increases or decreases.

Figure 5b illustrates the EIS spectra of hierarchical nanotube-constructed $\text{Na}_2\text{Ti}_3\text{O}_7$ materials prepared at temperatures of 120 °C (un-annealed) and 350 °C as well as an equivalent circuit (inset) used for fitting. As it is shown the impedance profiles comprise a depressed semicircle in high frequency range and a straight line at low frequency. From the plots is observed that due to annealing the impedance tends to decrease up to 156.5 Ω (NTO-350 sample). Taking into account sample geometry, the following values of resistivity were calculated by EIS fitting: 3.5 and 3.0 $\text{k}\Omega \cdot \text{cm}$ for the NTO-120 and NTO-350, respectively. The estimated conductivity of NTO-120 product is 2.88×10^{-4} S/cm. Annealing at 350 °C increases the conductivity up to 3.34×10^{-4} S/cm. The results are consistent with the UV-Vis data. The literature analysis indicates that the observed values are rather high. Indeed, as it was found in [45], the microparticulate $\text{Na}_2\text{Ti}_3\text{O}_7$ synthesized through the solid-state method has a conductivity of $1.19 \cdot 10^{-7}$ S/cm (after doping with ytterbium it is increased to $1.89 \cdot 10^{-7}$ S/cm). Table S2 presents the data calculated by modeling the experimental impedance spectra for studied materials.

3.2. Electrochemical Performance in Sodium Batteries of Self-Assembled Moss-like Hierarchical Architecture Constructed by $\text{Na}_2\text{Ti}_3\text{O}_7$ Nanotubes

Figure 6 shows CV curves of the NTO-120 and NTO-350 electrodes for the 1st, 4th, and 7th cycles. In general, no noticeable differences can be found between the graphs, which is explained by the identical electrochemical reaction mechanism. During the first cycle, a series of pronounced peaks near 1.93–2, 1.37–1.4, 0.86–0.94, and 0.54–0.56 V are detected in the cathodic sweep resulting from processes that occur at the electrode surface: the accumulation (adsorption) of sodium ionic species due to Faradic redox reactions (pseudocapacitive-like behavior) [46,47] and the decomposition of electrolyte with the formation of solid electrolyte interphase layer (SEI) [48]. The cathodic peak at 0.01–0.02 V corresponds to the insertion of Na^+ ions into the $\text{Na}_2\text{Ti}_3\text{O}_7$ crystal lattice accompanied by a formation of $\text{Na}_{2+x}\text{Ti}_3\text{O}_7$ and, meantime, reduction of a part of host Ti^{4+} ions to Ti^{3+} due to the charge compensation [46]. For the subsequent cycles, the contribution of irreversible processes reduces significantly, as shown in the cathodic scans of 4th and 7th CV curves. In the initial anode process, broad peaks near 0.7 and 1.2 V are observed in CVs of NTO-120 and NTO-350 samples. Upon cycling, the anodic region evolves: the peak located at 0.7 V becomes more intense (it is stabilized after the 4th cycle), whereas the peak at 1.2 V, on the contrary, decreases. According to the previous works [49,50], the region of lower potentials refers to the extraction of sodium ions from the $\text{Na}_2\text{Ti}_3\text{O}_7$ lattice with the oxidation of trivalent Ti to tetravalent. The decrease in intensity of peak around 1.2 V during cycling likely results from incompletely reversible adsorption of Na^+ ions in the pores of the materials and/or inside the nanotubes [46,47].

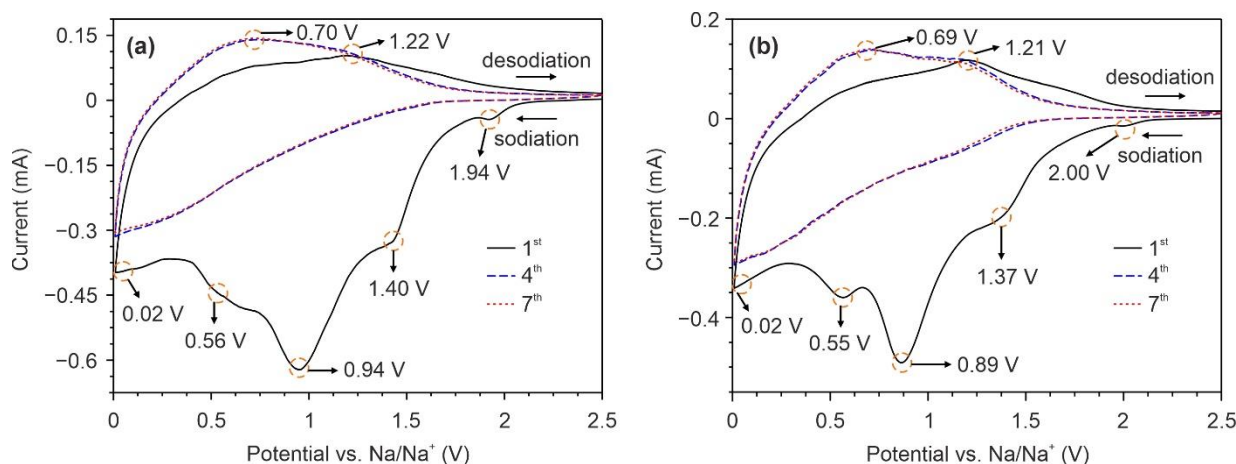
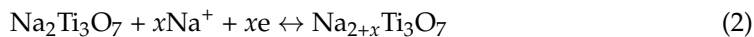


Figure 6. CV curves of NTO-120 (a) and NTO-350 (b) electrodes registered at a scan rate of 50 mV/s.

The results of galvanostatic charge/discharge tests for NTO-120 and NTO-350 electrodes at a current density of 50 mA/g (~ 0.3 C) are shown in Figure 7. As can be seen, the cycling data are consistent with that of CV studies. Indeed, the initial charge curves of both samples (Figure 7a,b) exhibit a number of inflections at the potentials close to positions of peaks in the first cathodic CV scans. The initial charge capacities of NTO-120 and NTO-350 are comparable and reach about 480 mA·h/g. During the first discharge process, the NTO-350 electrode delivers a specific capacity of 149 mA·h/g, higher than NTO-120 (125 mA·h/g). Analogously to CV measurements, noticeable irreversible losses are observed for samples mainly due to the electrolyte reduction and SEI film formation [51]. Next, the initial charge/discharge profiles differ from that of subsequent cycles. On the contrary, the curves of the 4th and the 7th cycles are almost coincident, implying the same electrochemical reaction mechanisms (Equation (2)). The reversible (discharge) specific capacities of analyzed materials after the 7th cycle are stabilized at approximately 127 mA·h/g (NTO-120) and 151 mA·h/g (NTO-350), which corresponds to deintercalation of about 1.4 and 1.7 sodium ions per formula unit of sodium titanate (x in Equation (2)).

The corresponding Coulombic efficiencies are equals to 84.8% and 86.9%. As it will be shown below (Figure 8a), such moderate efficiency in initial cycles is associated with the evolution of SEI layer.



where x is the amount of Na^+ incorporated into $\text{Na}_2\text{Ti}_3\text{O}_7$ matrix (can reach from 2 to 3.5 [35,52,53]).

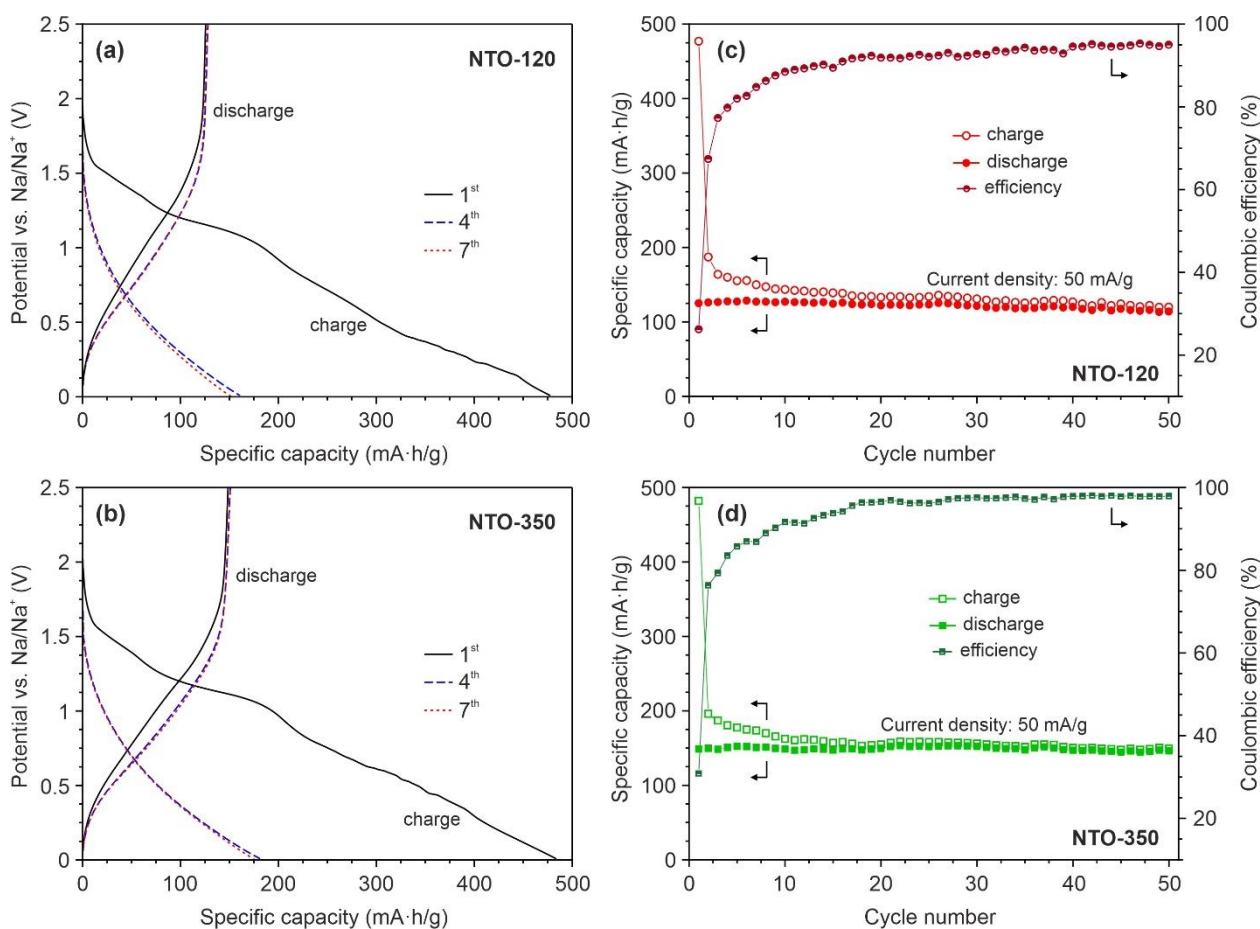


Figure 7. Charge-discharge voltage profiles of the 1st, 4th, and 7th initial cycles (a,b) and cycleability (c,d) for the NTO-120 and NTO-350 electrodes at a current density of 50 mA/g.

Figure 7c,d illustrates the evolution in specific capacities of tested materials during 50 charge/discharge cycles. The data show that upon cycling a slowdown in the rate of capacity degradation is observed for both electrodes. At the same time, it is clear that NTO-120 sample possesses a worse electrochemical performance. The drop in capacity of such electrode from the 7th to 50th cycle was about 10%, while for NTO-350 that did not exceed 3%. Observed differences in the behavior of NTO-120 and NTO-350 can probably be explained by unequal degree of dehydration. Indeed, according to TGA data (Figure S4), the total weight loss for NTO-120 and NTO-350 in the range from room temperature to 1000 °C is about 15.6 and 8.5%, respectively. Besides the water exists in various states in the analyzed products, namely absorbed molecules (the portion is the same for NTO-120 and NTO-350), free water, and H₂O molecules located in the interstitial cavities (only in un-annealed material). The literature overview reveals that free and coordinated water effects differently on the electrochemical performance in SIBs [54–58]. After the 50-fold cycling, the NTO-120 and NTO-350 maintained, respectively, around 114 and 146 mA·h/g. The corresponding Coulombic efficiencies increase to above 95.0 and 97.9%.

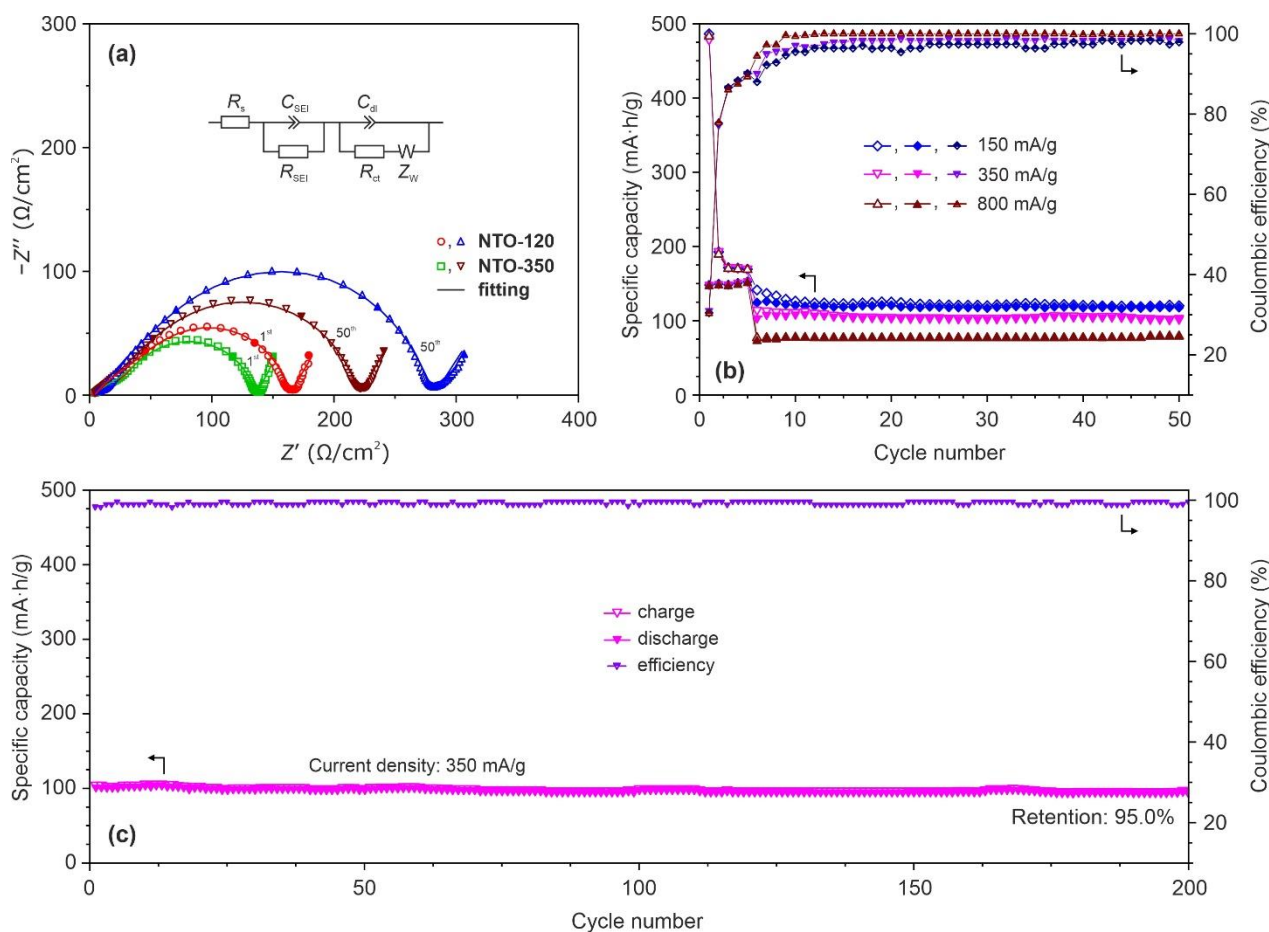


Figure 8. Impedance spectra registered at a fully sodiated state (at a potential of 0.01 V) during 1st and 50th cycles for analyzed materials (filled symbols denote the frequencies of 10^3 , 10^2 , and 10^{-2} Hz) with an electrical equivalent circuit (inset) applied for fitting (a), rate capability data (charge and discharge capacities are marked by filled and open symbols, Coulombic efficiencies are designated by semi-open symbols) after five initial formation cycles at 50 mA/g (b), and prolonged cycling performance at 350 mA/g (c) for the NTO-350 electrode.

Figure 8a depicts the EIS-spectra of NTO-120 and NTO-350 samples registered at a fully sodiated state (0.01 V) during 1st and 50th cycles.

The impedance spectra show depressed semicircles in the high-to-middle frequency range, followed by a low-frequency sloping line. It can be seen from graphs that upon cycling the radii of semicircles increase for both samples. At the same time, a difference in semicircles sizes is observed obviously from one to another studied materials. Moreover, it rose during cycling, as illustrated in EIS-plots. In order to analyze the observed features, next, the fitting of impedance curves was performed using the equivalent electric circuit (Figure 8a, inset) that involves the following components: R_s is the ohmic resistance of the cell, R_{SEI} and C_{SEI} are the resistance and geometric capacitance of a SEI film, R_{ct} and C_{dl} are the charge transfer resistance and double layer capacitance at an electrode/electrolyte interface, Z_W is the diffusion resistance. Note that bring of all of these elements into EES is dictated by the physical context within analyzed cells and supported by the goodness of fitting ($\chi^2 \leq 10^{-4}$). Table S3 represents the evolution of parameters for NTO-120 and NTO-350 based cells during cycling. The results show that in an initial period (first cycle) the NTO-350 possesses some lower values of R_{SEI} and R_{ct} (33.7 and 98.2 Ω/cm^2 , respectively) as compared to that of NTO-120 (51.4 and 108.0 Ω/cm^2). After the 50th cycle, the difference in the resistance of a SEI layer as well as in the charge transfer resistance between samples increases (NTO-350: $R_{SEI} = 65.5 \Omega/\text{cm}^2$, $R_{ct} = 151.8 \Omega/\text{cm}^2$; NTO-120: $R_{SEI} = 110.7 \Omega/\text{cm}^2$,

$R_{ct} = 167.2 \Omega/\text{cm}^2$). The obtained data correlate with that of CV-experiments (Figure 6) and charge/discharge tests (Figure 7). The same results without explanation were reported previously in [59] for the nanotubular $\text{Na}_2\text{Ti}_3\text{O}_7$ prepared at 130 and 150 °C. As seems, the observed features in electrochemical performance of such materials can be explained by different amounts of water. It is interesting to mention that before cycling (Figure S5), a relatively high impedance (exceeding those on the 1st and 50th cycles) of NTO-120 and NTO-350 samples is measured. Similar data were presented earlier in [42,59]. The observed phenomenon is explained by the fact that at the first cycle end most of the material's surface is covered with a SEI film reduces its surface energy and, hence, decreases the interfacial impedance (as supposed in [44]).

Rate capability experiments (Figure 8b) show that the performance of NTO-350 sample is stable under cycling with increased current densities. Indeed, it exhibits a reversible capacity of $\sim 118 \text{ mA}\cdot\text{h/g}$ (a capacity drops of about 19% as opposed to that at 50 mA/g) with a Coulombic efficiency of 97.9% at a cycling rate of 150 mA/g ($\sim 0.85 \text{ C}$). When the current load rises to 350 mA/g ($\sim 2 \text{ C}$), a discharge capacity drop of approximately 14% (to $\sim 102 \text{ mA}\cdot\text{h/g}$ at the 50th cycle) as well as a Coulombic efficiency growth to 98.3% were observed for NTO-350 electrode. Hence, the rate of capacity degradation from cycle to cycle slows down when an applied current density is increased. Similar behavior of $\text{Na}_2\text{Ti}_3\text{O}_7$ during cycling at higher rates is described in [50,51] and attributed to variations in SEI thickness or composition. When the NTO-350 was measured by 50 cycles of charge/discharge at a current density of 800 mA/g ($\sim 4.5 \text{ C}$), it exhibited approximately $79 \text{ mA}\cdot\text{h/g}$ with an almost 100% Coulombic efficiency.

Figure 8c displays the prolonged cycling performance of the NTO-350 electrode (continuation of the tests shown in Figure 8b) at a current load of 350 mA/g. Under continuous Na^+ ions insertion/extraction during 200 cycles the analyzed material keeps a considerable capacity of about $97 \text{ mA}\cdot\text{h/g}$ with the retention as high as 95.0% initial storage indicating its superior cyclic and adequate rate performances for SIBs.

4. Conclusions

In this work, we have developed an efficient strategy for the preparation of moss-like $\text{Na}_2\text{Ti}_3\text{O}_7$ frameworks assembled from ultrathin one-dimensional nanotubes with an outer diameter of 6–9 nm, a wall thickness of 2–3 nm, and a length of several hundred nanometers. The material has a unique structure similar to moss at the micro level and a high specific surface area ($314 \text{ m}^2/\text{g}$). The product is characterized by a porous texture ($0.54 \text{ cm}^3/\text{g}$) with a narrow pore size distribution near 5.7 nm. It was also found that the material is thermally stable up to 350 °C: its textural characteristics almost do not change (nanotube agglomeration was not observed), the specific area and pore volume after heat treatment remain at the level of $283 \text{ m}^2/\text{g}$ and $0.60 \text{ cm}^3/\text{g}$, respectively, pores with a diameter of 6.3 nm are predominated. It is found that the phase transformation of $\text{Na}_2\text{Ti}_3\text{O}_7$ into anatase occurs near 500 °C. The moss-like nanoarchitecture of sodium trititanate improves electrical conductivity reaching $2.88 \cdot 10^{-4} \text{ S/cm}$. Next, as it was found, heat treatment at 350 °C affects the electrical properties of $\text{Na}_2\text{Ti}_3\text{O}_7$: the conductivity increases three-fold to $3.34 \cdot 10^{-4} \text{ S/cm}$. The SIBs-type devices based on a hierarchically-organized nanotubular $\text{Na}_2\text{Ti}_3\text{O}_7$ possess promising cyclic and rate characteristics. A capacity of more than $95 \text{ mA}\cdot\text{h/g}$ after the 200th cycle is preserved even at a current density of 350 mA/g with a Coulombic efficiency of almost 100%. It was found that the degree of dehydration determines the electrochemical performance of the nanotubular $\text{Na}_2\text{Ti}_3\text{O}_7$. As we believed the reported strategy of hierarchically-organized $\text{Na}_2\text{Ti}_3\text{O}_7$ nanotubes may have a great potential for other fields (e.g., biomedicine, photocatalysis, and ion exchanger applications).

Supplementary Materials: The following supporting information can be downloaded at: <https://www.mdpi.com/article/10.3390/nano12111905/s1>, Figure S1: SEM-images at the magnifications of $378\times$ (a) and $17,180\times$ (b) for the NTO-350 sample; Figure S2: Close-up view for a white reindeer moss lichen from the Rondvassbu National Park (Norway, Europe). The photo was taken by Martin Schneider and is available for license from the iStock website; Figure S3: Elemental mapping of carbon for the NTO-120 material; Figure S4: Thermogravimetric analysis curves of the NTO-120 and NTO-350 samples; Figure S5: Nyquist plots of NTO-120 and NTO-350 electrodes before cycling (i.e., so-called «fresh» cells); Table S1: Method of synthesis and textural characteristics of some promising functional materials based on $\text{Na}_2\text{Ti}_3\text{O}_7$ [60–65]; Table S2: Calculated EIS parameters of NTO-120 and NTO-350 samples; Table S3: The EIS-spectra fitting results of NTO-120 and NTO-350 electrodes.

Author Contributions: D.P.O., A.I.N., S.L.S. and S.V.G. designed the study, participated in data analysis, discussed and analyzed experimental results, drafted the manuscript. D.P.O. and A.I.N. carried out the material laboratory work, interpreted the battery performance data. D.P.O. studied the optoelectronic properties of materials; A.B.P. measured and interpreted the electroconductive properties of products; V.G.K. carried out the microstructure characterization and elemental analysis; V.Y.M. studied the textural characteristics of materials; A.Y.U. collected and analyzed XPS data. All authors have read and agreed to the published version of the manuscript.

Funding: This work was supported by funding from the Russian Science Foundation (grant No. 19-73-10017).

Data Availability Statement: The data presented in this study are available on request from the corresponding author.

Acknowledgments: Electron-microscopic studies of the morphology and energy-dispersive X-ray analysis were carried out using the core facilities available at the A.V. Zhirmunsky National Scientific Center of Marine Biology FEB RAS and Institute of Chemistry FEB RAS (supported by the state assignment). For TGA experiments the authors are acknowledged Sc.D. D.V. Mashtalyar.

Conflicts of Interest: The authors declare no conflict of interest.

References

1. Moshnikov, V.A.; Gracheva, I.E.; Kuznezov, V.V.; Maximov, A.I.; Karpova, S.S.; Ponomareva, A.A. Hierarchical Nanostructured Semiconductor Porous Materials for Gas Sensors. *J. Non-Cryst. Solids* **2010**, *356*, 2020–2025. [\[CrossRef\]](#)
2. Xu, Y. Hierarchical Materials. In *Modern Inorganic Synthetic Chemistry*; Elsevier: Amsterdam, The Netherlands, 2017; pp. 545–574.
3. Noh, J.; Kwon, S.-H.; Park, S.; Kim, K.-K.; Yoon, Y.-J. TiO_2 Nanorods and Pt Nanoparticles under a UV-LED for an NO_2 Gas Sensor at Room Temperature. *Sensors* **2021**, *21*, 1826. [\[CrossRef\]](#) [\[PubMed\]](#)
4. Kuryavyi, V.G.; Ustinov, A.Y.; Opra, D.P.; Zverev, G.A.; Kaidalova, T.A. Composite Containing Nanosized Titanium Oxide and Oxyfluoride and Carbon Synthesized in Plasma of Pulse High-Voltage Discharge. *Mater. Lett.* **2014**, *137*, 398–400. [\[CrossRef\]](#)
5. Verma, V.; Al-Dossari, M.; Singh, J.; Rawat, M.; Kordy, M.G.M.; Shaban, M. A Review on Green Synthesis of TiO_2 NPs: Photocatalysis and Antimicrobial Applications. *Polymers* **2022**, *14*, 1444. [\[CrossRef\]](#) [\[PubMed\]](#)
6. Dell'Edera, M.; Lo Porto, C.; De Pasquale, I.; Petronella, F.; Curri, M.L.; Agostiano, A.; Comparelli, R. Photocatalytic TiO_2 -based coatings for environmental applications. *Catal. Today* **2021**, *380*, 62–83. [\[CrossRef\]](#)
7. Murugadoss, S.; Mühlhopt, S.; Diabaté, S.; Ghosh, M.; Paur, H.-R.; Stapf, D.; Weiss, C.; Hoet, P.H. Agglomeration State of Titanium-Dioxide (TiO_2) Nanomaterials Influences the Dose Deposition and Cytotoxic Responses in Human Bronchial Epithelial Cells at the Air-Liquid Interface. *Nanomaterials* **2021**, *11*, 3226. [\[CrossRef\]](#)
8. Chen, Z.; Han, S.; Zhou, S.; Feng, H.; Liu, Y.; Jia, G. Review of health safety aspects of titanium dioxide nanoparticles in food application. *NanoImpact* **2020**, *18*, 100224. [\[CrossRef\]](#)
9. Wu, X. Applications of Titanium Dioxide Materials. In *Titanium Dioxide*; IntechOpen: London, UK, 2021.
10. Qiu, G.; Guo, Y. Current Situation and Development Trend of Titanium Metal Industry in China. *Int. J. Miner. Metall. Mater.* **2022**, *29*, 599–610. [\[CrossRef\]](#)
11. El Khalloufi, M.; Drevelle, O.; Soucy, G. Titanium: An Overview of Resources and Production Methods. *Minerals* **2021**, *11*, 1425. [\[CrossRef\]](#)
12. Zeng, X.; Li, M.; Abd El-Hady, D.; Alshitari, W.; Al-Bogami, A.S.; Lu, J.; Amine, K. Commercialization of Lithium Battery Technologies for Electric Vehicles. *Adv. Energy Mater.* **2019**, *9*, 1900161. [\[CrossRef\]](#)
13. Chen, C.; Agrawal, R.; Wang, C. High Performance $\text{Li}_4\text{Ti}_5\text{O}_{12}/\text{Si}$ Composite Anodes for Li-Ion Batteries. *Nanomaterials* **2015**, *5*, 1469–1480. [\[CrossRef\]](#) [\[PubMed\]](#)
14. Mosa, J.; Aparicio, M. Sol-Gel Synthesis of Nanocrystalline Mesoporous $\text{Li}_4\text{Ti}_5\text{O}_{12}$ Thin-Films as Anodes for Li-Ion Microbatteries. *Nanomaterials* **2020**, *10*, 1369. [\[CrossRef\]](#)

15. Stenina, I.A.; Sobolev, A.N.; Kulova, T.L.; Yaroslavtsev, A.B. Effect of High-Molecular-Weight Carbon Sources on the Electrochemical Properties of $\text{Li}_4\text{Ti}_5\text{O}_{12}/\text{C}$ Composite Materials. *Inorg. Mater.* **2022**, *58*, 154–159. [[CrossRef](#)]
16. Sato, T.; Yoshikawa, K.; Zhao, W.; Kobayashi, T.; Rajendra, H.B.; Yonemura, M.; Yabuuchi, N. Efficient Stabilization of Na Storage Reversibility by Ti Integration into O'3-Type NaMnO_2 . *Energy Mater. Adv.* **2021**, *2021*, 1–12. [[CrossRef](#)]
17. Sun, Y.; Zheng, J.; Yang, Y.; Zhao, J.; Rong, J.; Li, H.; Niu, L. Design Advanced Porous Polyaniline-PEDOT:PSS Composite as High Performance Cathode for Sodium Ion Batteries. *Compos. Commun.* **2021**, *24*, 100674. [[CrossRef](#)]
18. Fatima, H.; Zhong, Y.; Wu, H.; Shao, Z. Recent Advances in Functional Oxides for High Energy Density Sodium-Ion Batteries. *Mater. Rep. Energy* **2021**, *1*, 100022. [[CrossRef](#)]
19. Park, G.D.; Cho, J.S.; Kang, Y.C. Sodium-Ion Storage Properties of Nickel Sulfide Hollow Nanospheres/Reduced Graphene Oxide Composite Powders Prepared by a Spray Drying Process and the Nanoscale Kirkendall Effect. *Nanoscale* **2015**, *7*, 16781–16788. [[CrossRef](#)]
20. Dai, Y.; Chen, Q.; Hu, C.; Huang, Y.; Wu, W.; Yu, M.; Sun, D.; Luo, W. Copper Fluoride as a Low-Cost Sodium-Ion Battery Cathode with High Capacity. *Chin. Chem. Lett.* **2022**, *33*, 1435–1438. [[CrossRef](#)]
21. Kulova, T. Causes of Germanium Phosphide Degradation under Prolonged Cycling. EIS Study. *Int. J. Electrochem. Sci.* **2022**, *17*, 2. [[CrossRef](#)]
22. Kulova, T.L.; Skundin, A.M. Germanium in Lithium-Ion and Sodium-Ion Batteries (A Review). *Russ. J. Electrochem.* **2021**, *57*, 1105–1137. [[CrossRef](#)]
23. Park, G.D.; Kim, J.H.; Park, S.-K.; Kang, Y.C. MoSe_2 Embedded CNT-Reduced Graphene Oxide Composite Microsphere with Superior Sodium Ion Storage and Electrocatalytic Hydrogen Evolution Performances. *ACS Appl. Mater. Interfaces* **2017**, *9*, 10673–10683. [[CrossRef](#)] [[PubMed](#)]
24. Cheng, H.; Garcia-Araez, N.; Hector, A.L. Synthesis of Vanadium Nitride–Hard Carbon Composites from Cellulose and Their Performance for Sodium-Ion Batteries. *ACS Appl. Energy Mater.* **2020**, *3*, 4286–4294. [[CrossRef](#)]
25. Wang, Y.; Zhu, W.; Guerfi, A.; Kim, C.; Zaghbi, K. Roles of Ti in Electrode Materials for Sodium-Ion Batteries. *Front. Energy Res.* **2019**, *7*, 28. [[CrossRef](#)]
26. Wang, W.; Liu, Y.; Wu, X.; Wang, J.; Fu, L.; Zhu, Y.; Wu, Y.; Liu, X. Advances of TiO_2 as Negative Electrode Materials for Sodium-Ion Batteries. *Adv. Mater. Technol.* **2018**, *3*, 1800004. [[CrossRef](#)]
27. Doeff, M.M.; Cabana, J.; Shirpour, M. Titanate Anodes for Sodium Ion Batteries. *J. Inorg. Organomet. Polym. Mater.* **2014**, *24*, 5–14. [[CrossRef](#)]
28. Opra, D.P.; Gnedenkov, S.V.; Sinebryukhov, S.L.; Gerasimenko, A.V.; Ziatdinov, A.M.; Sokolov, A.A.; Podgorbunsky, A.B.; Ustinov, A.Y.; Kuryavyi, V.G.; Mayorov, V.Y.; et al. Enhancing Lithium and Sodium Storage Properties of TiO_2 (B) Nanobelts by Doping with Nickel and Zinc. *Nanomaterials* **2021**, *11*, 1703. [[CrossRef](#)]
29. Stenina, I.A.; Kozina, L.D.; Kulova, T.L.; Skundin, A.M.; Chekannikov, A.A.; Yaroslavtsev, A.B. Synthesis and Ionic Conduction of Sodium Titanate $\text{Na}_2\text{Ti}_3\text{O}_7$. *Russ. J. Inorg. Chem.* **2016**, *61*, 1235–1240. [[CrossRef](#)]
30. Dynarowska, M.; Kotwiński, J.; Leszczynska, M.; Marzantowicz, M.; Krok, F. Ionic Conductivity and Structural Properties of $\text{Na}_2\text{Ti}_3\text{O}_7$ Anode Material. *Solid State Ionics* **2017**, *301*, 35–42. [[CrossRef](#)]
31. Zima, T.M.; Baklanova, N.I.; Utkin, A.V. Hydrothermal Synthesis of a Nanostructured TiO_2 -Based Material in the Presence of Chitosan. *Inorg. Mater.* **2012**, *48*, 821–826. [[CrossRef](#)]
32. Kim, G.-S.; Kim, Y.-S.; Seo, H.-K.; Shin, H.-S. Hydrothermal Synthesis of Titanate Nanotubes Followed by Electrodeposition Process. *Korean J. Chem. Eng.* **2006**, *23*, 1037–1045. [[CrossRef](#)]
33. Jing, M.; Li, J.; Han, C.; Yao, S.; Zhang, J.; Zhai, H.; Chen, L.; Shen, X.; Xiao, K. Electrospinning Preparation of Oxygen-Deficient Nano TiO_{2-x} /Carbon Fibre Membrane as a Self-Standing High Performance Anode for Li-Ion Batteries. *R. Soc. Open Sci.* **2017**, *4*, 170323. [[CrossRef](#)] [[PubMed](#)]
34. Opra, D.P.; Gnedenkov, S.V.; Sinebryukhov, S.L.; Podgorbunsky, A.B.; Sokolov, A.A.; Ustinov, A.Y.; Kuryavyi, V.G.; Mayorov, V.Y.; Zheleznov, V.V. Doping of Titania with Manganese for Improving Cycling and Rate Performances in Lithium-Ion Batteries. *Chem. Phys.* **2020**, *538*, 110864. [[CrossRef](#)]
35. Ni, J.; Fu, S.; Wu, C.; Zhao, Y.; Maier, J.; Yu, Y.; Li, L. Superior Sodium Storage in $\text{Na}_2\text{Ti}_3\text{O}_7$ Nanotube Arrays through Surface Engineering. *Adv. Energy Mater.* **2016**, *6*, 1502568. [[CrossRef](#)]
36. An, Y.; Li, Z.; Xiang, H.; Huang, Y.; Shen, J. First-Principle Calculations for Electronic Structure and Bonding Properties in Layered $\text{Na}_2\text{Ti}_3\text{O}_7$. *Open Phys.* **2011**, *9*, 1488–1492. [[CrossRef](#)]
37. Araújo-Filho, A.A.; Silva, F.L.R.; Righi, A.; da Silva, M.B.; Silva, B.P.; Caetano, E.W.S.; Freire, V.N. Structural, Electronic and Optical Properties of Monoclinic $\text{Na}_2\text{Ti}_3\text{O}_7$ from Density Functional Theory Calculations: A Comparison with XRD and Optical Absorption Measurements. *J. Solid State Chem.* **2017**, *250*, 68–74. [[CrossRef](#)]
38. Zhang, Z.; Goodall, J.B.M.; Brown, S.; Karlsson, L.; Clark, R.J.H.; Hutchison, J.L.; Rehman, I.U.; Darr, J.A. Continuous Hydrothermal Synthesis of Extensive 2D Sodium Titanate ($\text{Na}_2\text{Ti}_3\text{O}_7$) Nano-Sheets. *Dalt. Trans.* **2010**, *39*, 711–714. [[CrossRef](#)]
39. Garay-Rodríguez, L.F.; Murcia-López, S.; Andreu, T.; Moctezuma, E.; Torres-Martínez, L.M.; Morante, J.R. Photocatalytic Hydrogen Evolution Using Bi-Metallic (Ni/Pt) $\text{Na}_2\text{Ti}_3\text{O}_7$ Whiskers: Effect of the Deposition Order. *Catalysts* **2019**, *9*, 285. [[CrossRef](#)]
40. Wang, B.L.; Chen, Q.; Wang, R.H.; Peng, L.-M. Synthesis and Characterization of $\text{K}_2\text{Ti}_6\text{O}_{13}$ Nanowires. *Chem. Phys. Lett.* **2003**, *376*, 726–731. [[CrossRef](#)]

41. Pan, H.; Lu, X.; Yu, X.; Hu, Y.-S.; Li, H.; Yang, X.-Q.; Chen, L. Sodium Storage and Transport Properties in Layered Na₂Ti₃O₇ for Room-Temperature Sodium-Ion Batteries. *Adv. Energy Mater.* **2013**, *3*, 1186–1194. [[CrossRef](#)]
42. Fu, S.; Ni, J.; Xu, Y.; Zhang, Q.; Li, L. Hydrogenation Driven Conductive Na₂Ti₃O₇ Nanoarrays as Robust Binder-Free Anodes for Sodium-Ion Batteries. *Nano Lett.* **2016**, *16*, 4544–4551. [[CrossRef](#)]
43. Vithal, M.; Rama Krishna, S.; Ravi, G.; Palla, S.; Velchuri, R.; Pola, S. Synthesis of Cu²⁺ and Ag⁺ Doped Na₂Ti₃O₇ by a Facile Ion-Exchange Method as Visible-Light-Driven Photocatalysts. *Ceram. Int.* **2013**, *39*, 8429–8439. [[CrossRef](#)]
44. Singh, M.; Goyal, M.; Devlal, K. Size and Shape Effects on the Band Gap of Semiconductor Compound Nanomaterials. *J. Taibah Univ. Sci.* **2018**, *12*, 470–475. [[CrossRef](#)]
45. Xia, J.; Zhao, H.; Pang, W.K.; Yin, Z.; Zhou, B.; He, G.; Guo, Z.; Du, Y. Lanthanide Doping Induced Electrochemical Enhancement of Na₂Ti₃O₇ Anodes for Sodium-Ion Batteries. *Chem. Sci.* **2018**, *9*, 3421–3425. [[CrossRef](#)] [[PubMed](#)]
46. Chen, C.-C.; Zhang, N.; Liu, Y.-C.; Wang, Y.-J.; Chen, J. In-Situ Preparation of Na₂Ti₃O₇ Nanosheets as High-Performance Anodes for Sodium Ion Batteries. *Acta Phys.-Chim. Sin.* **2016**, *32*, 349–355. [[CrossRef](#)]
47. Ko, J.S.; Doan-Nguyen, V.V.T.; Kim, H.-S.; Muller, G.A.; Serino, A.C.; Weiss, P.S.; Dunn, B.S. Na₂Ti₃O₇ Nanoplatelets and Nanosheets Derived from a Modified Exfoliation Process for Use as a High-Capacity Sodium-Ion Negative Electrode. *ACS Appl. Mater. Interfaces* **2017**, *9*, 1416–1425. [[CrossRef](#)]
48. Wang, C.; Yang, Y.; Chen, Z.; He, C.; Su, J.; Wen, Y. A Mild Process for the Synthesis of Na₂Ti₃O₇ as an Anode Material for Sodium-Ion Batteries in Deep Eutectic Solvent. *J. Mater. Sci. Mater. Electron.* **2019**, *30*, 8422–8427. [[CrossRef](#)]
49. Rudola, A.; Sharma, N.; Balaya, P. Introducing a 0.2 V Sodium-Ion Battery Anode: The Na₂Ti₃O₇ to Na_{3-x}Ti₃O₇ Pathway. *Electrochem. Commun.* **2015**, *61*, 10–13. [[CrossRef](#)]
50. Zukalová, M.; Pitřna Lásková, B.; Mocek, K.; Zukal, A.; Bouša, M.; Kavan, L. Electrochemical Performance of Sol-Gel-Made Na₂Ti₃O₇ Anode Material for Na-Ion Batteries. *J. Solid State Electrochem.* **2018**, *22*, 2545–2552. [[CrossRef](#)]
51. Kuz'mina, A.A.; Kudryashova, Y.O.; Kulova, T.L.; Skundin, A.M.; Chekannikov, A.A. Degradation Mechanism of Electrodes from Sodium Titanate at Cycling. *Electrochem. Energy* **2019**, *19*, 148–156. [[CrossRef](#)]
52. Wang, W.; Yu, C.; Lin, Z.; Hou, J.; Zhu, H.; Jiao, S. Microspheric Na₂Ti₃O₇ Consisting of Tiny Nanotubes: An Anode Material for Sodium-Ion Batteries with Ultrafast Charge–Discharge Rates. *Nanoscale* **2013**, *5*, 594–599. [[CrossRef](#)]
53. Chen, Z.; Lu, L.; Gao, Y.; Zhang, Q.; Zhang, C.; Sun, C.; Chen, X. Effects of F-Doping on the Electrochemical Performance of Na₂Ti₃O₇ as an Anode for Sodium-Ion Batteries. *Materials* **2018**, *11*, 2206. [[CrossRef](#)] [[PubMed](#)]
54. Dubouis, N.; Serva, A.; Salager, E.; Deschamps, M.; Salanne, M.; Grimaud, A. The Fate of Water at the Electrochemical Interfaces: Electrochemical Behavior of Free Water Versus Coordinating Water. *J. Phys. Chem. Lett.* **2018**, *9*, 6683–6688. [[CrossRef](#)] [[PubMed](#)]
55. Wu, J.; Song, J.; Dai, K.; Zhuo, Z.; Wray, L.A.; Liu, G.; Shen, Z.; Zeng, R.; Lu, Y.; Yang, W. Modification of Transition-Metal Redox by Interstitial Water in Hexacyanometalate Electrodes for Sodium-Ion Batteries. *J. Am. Chem. Soc.* **2017**, *139*, 18358–18364. [[CrossRef](#)] [[PubMed](#)]
56. Li, Y.; Feng, X.; Cui, S.; Shi, Q.; Mi, L.; Chen, W. From α-NaMnO₂ to Crystal Water Containing Na-Birnessite: Enhanced Cycling Stability for Sodium-Ion Batteries. *Cryst. Eng. Commun.* **2016**, *18*, 3136–3141. [[CrossRef](#)]
57. Liu, Z.; Tian, R.; Mushtaq, M.; Guo, W.; Yao, M.; Feng, J. Performance Modulation through Synergetic Effect of Interstitial Water with Ti-Substitution for Sodium Ion Battery Cathode. *Chem. Lett.* **2019**, *48*, 670–673. [[CrossRef](#)]
58. Song, J.; Wang, L.; Lu, Y.; Liu, J.; Guo, B.; Xiao, P.; Lee, J.-J.; Yang, X.-Q.; Henkelman, G.; Goodenough, J.B. Removal of Interstitial H₂O in Hexacyanometallates for a Superior Cathode of a Sodium-Ion Battery. *J. Am. Chem. Soc.* **2015**, *137*, 2658–2664. [[CrossRef](#)]
59. Ding, M. Preparation of Thin-Walled Na₂Ti₃O₇ Nanotube and Its Electrochemical Properties. *Int. J. Electrochem. Sci.* **2021**, *16*. [[CrossRef](#)]
60. Zhou, Z.; Xiao, H.; Zhang, F.; Zhang, X.; Tang, Y. Solvothermal Synthesis of Na₂Ti₃O₇ nanowires Embedded in 3D Graphene Networks as an Anode for High-Performance Sodium-Ion Batteries. *Electrochim. Acta* **2016**, *211*, 430–436. [[CrossRef](#)]
61. Song, T.; Ye, S.; Liu, H.; Wang, Y.G. Self-Doping of Ti³⁺ into Na₂Ti₃O₇ increases Both Ion and Electron Conductivity as a High-Performance Anode Material for Sodium-Ion Batteries. *J. Alloys Compd.* **2018**, *767*, 820–828. [[CrossRef](#)]
62. Zhong, W.; Tao, M.; Tang, W.; Gao, W.; Yang, T.; Zhang, Y.; Zhan, R.; Bao, S.-J.; Xu, M. MXene-Derivative Pompon-like Na₂Ti₃O₇@C Anode Material for Advanced Sodium Ion Batteries. *Chem. Eng. J.* **2019**, *378*, 122209. [[CrossRef](#)]
63. Chen, S.; Gao, L.; Zhang, L.; Yang, X. Mesoporous Na₂Ti₃O₇ Microspheres with Rigid Framework as Anode Materials for High-Performance Sodium Ion Batteries. *Ionics* **2019**, *25*, 2211–2219. [[CrossRef](#)]
64. Vattikuti, S.V.P.; Reddy, P.A.K.; NagaJyothi, P.C.; Shim, J.; Byon, C. Hydrothermally Synthesized Na₂Ti₃O₇ Nanotube–V₂O₅ Heterostructures with Improved Visible Photocatalytic Degradation and Hydrogen Evolution—Its Photocorrosion Suppression. *J. Alloys Compd.* **2018**, *740*, 574–586. [[CrossRef](#)]
65. Hayashi, H.; Nakamura, T.; Ebina, T. Hydrothermal Synthesis of Sodium Titanate Nanosheets Using a Supercritical Flow Reaction System. *J. Ceram. Soc. Japan* **2016**, *124*, 74–78. [[CrossRef](#)]